Hydrodynamic loadings on a horizontal axis tidal turbine prototype

Pablo Ouro[a], Magnus Harrold[b], Thorsten Stoesser[a,*], Peter Bromley[b]

[a]*Hydro-environmental Research Centre, Cardiff School of Engineering, Cardiff University. The Parade CF24 3AA, Cardiff, UK*
[b]*Tidal Energy Ltd, CF23 8RS Cardiff, UK.*

Abstract

Until recently tidal stream turbine design has been carried out mainly by experimental prototype testing aiming at maximum turbine efficiency. The harsh and highly turbulent environments in which tidal stream turbines operate in poses a design challenge mainly with regards to survivability of the turbine owing to the fact that tidal turbines are exposed to significant intermittent hydrodynamic loads. Credible numerical models can be used as a complement to experiments during the design process of tidal stream turbines. They can provide insights into the hydrodynamics, predict tidal turbine performance and clarify their fluid-structure interaction as well as quantify the hydrodynamic loadings on the rotor. The latter can lead to design enhancements aiming at increased robustness and survivability of the turbine. Physical experiments and complementary large-eddy simulations of flow around a horizontal axis tidal turbine rotor are presented. The goal is to provide details of the hydrodynamics around the rotor, the performance of the turbine and acting hydrodynamic forces on the rotor blades. The simulation results are first compared with the experimental and good agreement between measured and simulated coefficients of power are obtained. Acting bending and torsional moment coefficients on the blade-hub junction are computed for idealised flow conditions. Finally, realistic

---

*Corresponding author: Stoesser@cardiff.ac.uk
Email addresses: `OuroBarbaP@cardiff.ac.uk` (Pablo Ouro), `Magnus.Harrold@tidalenergyltd.com` (Magnus Harrold), `Stoesser@cardiff.ac.uk` (Thorsten Stoesser), `Peter.Bromley@tidalenergyltd.com` (Peter Bromley)

environmental turbulence is added to the inflow and its impact on the turbine's performance, hydrodynamics and rotor loadings is quantified.

1. Introduction

The predictability of tides is a virtue and it allows predicting far in advance and with high accuracy the energy that can be extracted from this renewable energy resource. Great Britain is endowed with vast tidal energy resources, a large tidal range (of up to 14m in the Severn Estuary), thousands of kilometers of coastline, featuring narrow straits or headlands which often result in powerful tidal streams. Tidal streams are harnessed through the deployment of tidal turbines, basically under water windmills and presently, Horizontal Axis Tidal Turbines (HATT) constitute the majority of commercialised turbines. It appears that some technology is imported directly from Horizontal Axis Wind Turbines (HAWT) [1], however, water is approximately 800 times denser than air and therefore water causes significantly greater loads on HATT rotors compared to their HAWT counterpart. Consequently, essential modifications in the tidal stream turbine's design are needed to avoid structural failures, e.g. shorter and thicker blades and hence a smaller rotor diameter, and this has been subject of research from the beginning.

Early experimental works on HATTs have focused mainly on their hydrodynamics and performance. Bahaj et al. [2] studied the effect of free surface proximity, yaw angle and different flow speeds on the performance of a tidal turbine. Mycek et al. [3] studied the wake produced downstream of the turbine and its interaction with other turbine(s) towards the design of tidal stream turbine farms, and complementary to this Vennell et al. [4] presented their vision of the future of large tidal turbine farms. With a more hydrodynamic loadings focus, Milne et al. [5] investigated the structural moments of a 3-bladed HATT subjected to a sinusoidal motion under uniform flow conditions, and Blackmore

2

et al. [6] studied the influence of different turbulence intensities and eddy length scales in the approach flow on the turbine loadings and performance.

There has been increasing interest in developing numerical methods that can reproduce the complex flow in the near field of tidal turbines. These can be used in parallel to laboratory experiments or field tests because they can provide more detailed information on the near-field hydrodynamics or can predict turbine performance data for alternative rotor designs. Early works employed the blade element method (BEM) and the actuator disk theory. However, the latter does not consider the flow unsteadiness and the former discretises the turbine's geometry by a set of single points representing blade sections with constant hydrodynamic coefficients. Such simplifications resulted in methods which are computationally cheap and these approaches gave good results for the turbine's far field [7, 8] however they are unable to reproduce the physics around the turbine rotor.

The complex and highly turbulent flow around tidal turbines is governed by fluid-structure interaction including dynamic stall, trailing vortex wake generation or hydrodynamic load unsteadiness. Advanced and accurate models, such as blade resolved methods, are needed to simulate these features [9]. In general, blade resolved methods use three-dimensional meshes that represent explicitly the turbine's geometry and motion and the flow field is computed using Reynolds Averaged Navier-Stokes (RANS) or Large-Eddy Simulation (LES). RANS models are widely used as the computational requirements are affordable [10, 11] though the time-averaging of the velocity field does not accomplish a realistic representation of the instantaneous fluid-blade interaction. On the other hand, LES resolves the large-scale flow structures present in the velocity field [12] as the so-called dynamic stall [13]. The main drawback of LES is the large amount of computational resources required to run the demanded fine meshes although exponentially increasing computational resources is making LES more accessible to the research community [14].

There have been only few studies applying LES to study the hydrodynamics and performance of HATTs. Kang et al. [15] were the first to reproduce nu-

3

merically the operation of a commercial HATT prototype using the immersed boundary method. McNaughton et al. [16] and Bai et al. [17] performed LES of the experimental setup from Bahaj et al. [2], and whilst [16] used a sliding mesh method, [17] employed the immersed boundary method. In all three studies an excellent match with the experimental data was achieved showing the potential and accuracy of the method of LES.

The Immersed Boundary (IB) method has demonstrated great potential for the simulation of fluid-structure interaction (FSI). The IB method was first introduced by Peskin [18] to simulate the FSI of heart valves. Some of the main advantages of the IB method are: the reduction of computational effort in the simulations compared to body-fitted and/or sliding mesh methods by avoiding remeshing and variable re-allocation at each time step or the ability to employ fast (multi-grid) Poisson equation solvers. Different IB methods have been developed since [18] and are mainly divided depending on whether the body geometry is considered as a continuous surface or discretised into a finite set of points or markers. While Kang et at. [15] and Bai et al. [17] used a continuum IB method, in the following the discrete method developed by Fadlun et al. [19] and improved by Uhlmann [20], the so-called direct forcing IB method, is adopted for the simulations. This method has been validated previously for vertical axis tidal turbines [21, 22], particle laden flows [20], bluff body representation [23], and several other applications as summarised in [24].

During the lifetime of tidal turbines, they are subjected to harsh and highly turbulent environmental conditions. This compromises their structural design in order to avoid any major failure during the project lifespan or at least reduce as much as possible the costly in site maintenance by reducing risks. Therefore, it is essential to identify and quantify the main stresses on the turbine. To date only few research has been dedicated to tidal turbine loadings due to the inherent difficulty of experimentally determining acting forces [25]. Nichols-Lee et al. [26] determined structural loads on the blades made of composite materials while Blackmore et al. [6] focused on the effect of turbulence on hydrodynamic loads on a HATT. Numerical studies that quantified hydrodynamic loadings of

4

tidal turbines have been presented by Mason-Jones et al. [11], Frost et al. [10] and Tatum et al. [27]. These studies were carried out using RANS models which, due to its time-averaging nature, can not resolve the details of the instantaneous flow.

In the research reported in this paper, a LES-based numerical approach together with the IB method is employed for the simulation of the fluid-structure interaction of a HATT. LES is able to resolve explicitly the large, energetic scales in the flow and hence is expected to provide unprecedented details of the FSI of a HATT rotor subjected to turbulent flow. The method is first validated with data from experimental tests of a HATT prototype. This is followed by revelation of hydrodynamic details of the near-wake of the HATT rotor. Then hydrodynamic loads are quantified in terms of bending and torsional moments at the blade root. Finally, the effect of oncoming environmental turbulence on the turbine's performance and its structural moments is quantified.

2. Experimental study

Ahead of sea deployment, the performance and control strategy of a 1:30-scale commercial horizontal axis tidal turbine model was tested [28]. The 0.4m diameter (D) turbine prototype was placed in a $15m$ long, $1.20m$ wide and $1.0m$ deep recirculating flume located in Cardiff University's hydraulics laboratory. The turbine was suspended in the tank from a Y-shaped frame that was fixed to a platform sitting above the flume, leaving the rotor positioned approximately in the center of the tank's cross-section. The rotor blades were 3D printed and fitted with circular pins to position into holes on the circumference of the turbine hub. The correct pitch angles were set by resting the blades on 3D printed molds aligned with the back of the hub. Once the pitch angles were set, screws inside the hub were tightened to prevent the pins from moving. The model turbine in the flume is depicted in Fig. 1.

The turbine was controlled via a programmable servomotor, used previously for similar tidal turbine tests [29, 30], and hydrodynamic loads from the rotor
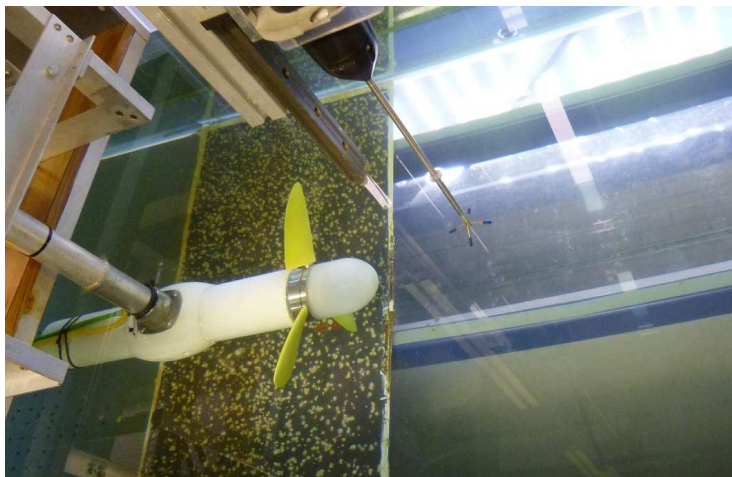
Figure 1: The 1:30-scale HATT prototype mounted in the flume in Cardiff University's hydraulics laboratory.

were opposed by the torque of the servomotor. The software that accompanied the servomotor drive allowed the turbine to be controlled in either rotational speed or torque mode. Measurement data of these two parameters were sampled at 10Hz. A detailed description of the servomotor and its method of operation can be found in [31].

A Nortek Acoustic Doppler Velocimeter (ADV) positioned upstream and in line with the centre of the rotor was used to measure the flow velocity in the tank. The instrument was configured to sample at 25Hz, with all measurements subsequently quality controlled for low correlation and signal to noise ratios (SNR) in post-processing. Additionally, any measurements found to be outside ± 3 standard deviations from the mean value were removed. Fig. 2 shows a 300s sample of the streamwise velocity with a bulk velocity of U_0=0.76m/s and a water depth of H=0.66m. A free-stream turbulence intensity I=10% was found from the sample and used in the further numerical analysis aiming at investigating the effect of realistic inflow turbulence on the turbine's performance and hydrodynamic loads.
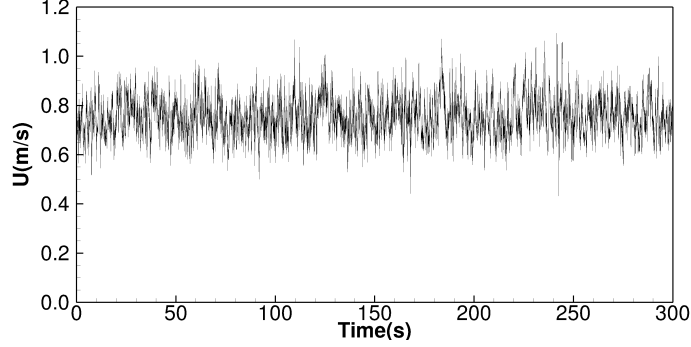
6

Figure 2: Streamwise velocity signal obtained with ADV placed upstream the turbine for 300s.

3. Numerical framework, Setup and Validation

3.1. Governing equations

The numerical simulations are carried out with Hydro3D, an in-house Large-Eddy Simulation (LES) code that has been validated and applied to a number of complex flows including vertical axis tidal turbines [21, 22], bubble plumes [32, 33] and hydraulic structures [34, 35, 36, 37]. Hydro3D solves the spatially filtered Navier-Stokes equations for turbulent, incompressible, three-dimensional flow field, which read:

$$\nabla \mathbf{u} = 0 \tag{1}$$

$$\frac{\partial \mathbf{u}}{\partial t} + \mathbf{u} \cdot \nabla \mathbf{u} = -\nabla p + \nu \nabla^2 \mathbf{u} - \nabla \boldsymbol{\tau} + \boldsymbol{f} \tag{2}$$

where $\mathbf{u}$ and p are the fluid velocity and pressure, ν is the fluid kinematic viscosity and $\boldsymbol{f}$ is a forcing term of the immersed boundary (IB) method detailed below. The sub-grid scale stress tensor, $\boldsymbol{\tau}$, is computed using the WALE model of Nicoud et al. [38]. The Eulerian fluid domain is discretised with a fourth-order central finite difference scheme with staggered storage of the velocity components on a Cartesian grid. A combination of a third-order low-storage Runge-Kutta and Crank-Nicolson methods for convective and diffusive terms respectively are used in the prediction step of the present fractional-step method [39, 40]. The solution of a Poisson pressure-correction equation

7

is achieved using a multi-grid technique in the final step as a corrector of the predicted velocities. Recent developments in Hydro3D such as local mesh refinement [41] and a hybrid MPI-OpenMP parallelisation scheme [32] have increased the code's capabilities to perform expensive simulations on high-performance computers.

A refined direct forcing IB method [20, 35] is adopted for the representation of solid bodies due to its ability to handle complex moving geometries within a fixed fluid domain. The moving bodies are represented as a set of Lagrangian markers or points that conform the desired geometry (see Section 3.2). In this Eulerian (fluid)-Lagrangian (solid) framework the communication of velocities and forces (solid on fluid and vice versa) is achieved via delta functions (δ), which are herein reconstructed using the kernel ϕ_3^* proposed by Yang et al. [42]. Using these delta functions, the predicted fluid velocity ($\mathbf{u}_i$) is transferred to each Lagrangian marker L from their closest n_e fluid nodes to obtain the interpolated Lagrangian velocity, $\mathbf{U}_L$, as,

$$\mathbf{U}_L = \sum_{i=1}^{n_e} \mathbf{u}_i \cdot \delta(\mathbf{x}_i - \mathbf{X}_L) \cdot \Delta\mathbf{x}_i \tag{3}$$

The Lagrangian force at each marker ($\boldsymbol{F}_L$) is computed as the difference between the desired velocity at the marker ($\mathbf{U_L^*} = \partial\boldsymbol{X}_L/\partial t$) and the interpolated Lagrangian velocity via,

$$\mathbf{F}_L = \frac{\mathbf{U}_L^* - \mathbf{U}_L}{\Delta t} \tag{4}$$

Finally, the Lagrangian force is then transferred back onto the neighbouring fluid cells using the previous delta functions as,

$$\boldsymbol{f}(\mathbf{x}_i) = \sum_{L=1}^{n_L} \mathbf{F}_L \cdot \delta(\mathbf{X}_L - \mathbf{x}_i) \cdot \Delta V_L \tag{5}$$

where $\mathbf{x}_i$ and $\mathbf{u}_i$ are the coordinates and velocities of the fluid cell i, $\mathbf{X}_L$ and $\mathbf{U}_L$ are the coordinates and velocities of the Lagrangian marker L, and n_e and n_L are the number of Eulerian neighbours to each solid marker and vice versa determined from the width of the kernel used in the interpolation [42]. Δt is

the time step and $\Delta\mathbf{x}_i = \Delta x \cdot \Delta y \cdot \Delta z$ is the volume of an Eulerian cell [21]. The chosen direct forcing method demands that both solid and fluid meshes have approximately the same resolution to ensure that exchanged forces between the different frameworks (Eulerian/Lagrangian) are consistent.

3.2. Simulation of turbine rotation

The HATT geometry is generated by a discrete mesh using Delaunay triangulation featuring a resolution similar to the Eulerian fluid mesh ($\Delta\mathbf{x}_i \approx \Delta V_L$). The chosen direct forcing method demands that both solid and fluid meshes have approximately the same resolution to ensure that exchanged forces between the different frameworks (Eulerian/Lagrangian) are consistent. This is achieved by placing approximately one IB point every mesh cell. The nodes of the generated unstructured grid are adopted as the Lagrangian markers representing the turbine's geometry. In an attempt to reduce the computational effort, the length of the hub was shortened compared to the real prototype dimensions. The influence of the length of the hub is deemed small, which was also demonstrated by Kang et al. [15]. The turbine rotates counter-clockwise with a prescribed constant rotational velocity (Ω) around the centre $\boldsymbol{C}$ (C_x, C_y, C_z), as indicated in Fig. 3a). As a first step, the initial local Cartesian coordinates ($\mathbf{X}_{L_0} = (X_{L_0}, Y_{L_0}, Z_{L_0})^T$), the initial described angle ($\theta_{L_0} = \mathrm{atan}(Y_{L_0}/Z_{L_0})$) and the radius ($R_L = \sqrt{(Y_{L_0})^2 + (Z_{L_0})^2}$) of each marker are calculated. The rotated angle of each marker moving at a constant Ω at the time t is $\theta_L(t) = \theta_{0_L} + \Omega t$, and thus its position is calculated as,

$$\mathbf{X}_L = \begin{pmatrix} X_L \\ Y_L \\ Z_L \end{pmatrix} = \begin{pmatrix} C_x \\ C_y \\ C_z \end{pmatrix} + \begin{pmatrix} X_{L_0} \\ R_L \cdot \sin(\theta_L(t)) \\ R_L \cdot \cos(\theta_L(t)) \end{pmatrix} \tag{6}$$

The force vector, $\mathbf{F}$, per blade is the sum of all forces from the markers comprising that blade and is computed as follows,

$$\mathbf{F} = (F_x, F_y, F_z) = \int_{blade} \rho\mathbf{F}_L dV_L = \int_{blade} \rho(F_{x_L}, F_{y_L}, F_{z_L}) dV_L \tag{7}$$

9

The x-component of $\mathbf{F}$ will be hereinafter referred as the thrust force, T. The torque, Q, generated by the turbine is computed from the y- and z-force components as,

$$Q = \sum_{L=1}^{N_L} (F_{y_L} \cdot cos(\theta_L) + F_{z_L} \cdot sin(\theta_L)) \cdot R_L \tag{8}$$

The power coefficient, C_P, is the ratio of generated turbine power, P_T, calculated as torque times rotational speed, to the power available in the water, P_W,

$$C_P = \frac{P_T}{P_W} = \frac{Q \cdot \Omega}{1/2 \rho U_0^3 A} \tag{9}$$

where U_0 is the free-stream water velocity, ρ is the water density and $A = \pi \cdot R^2$ is the rotor's swept area.
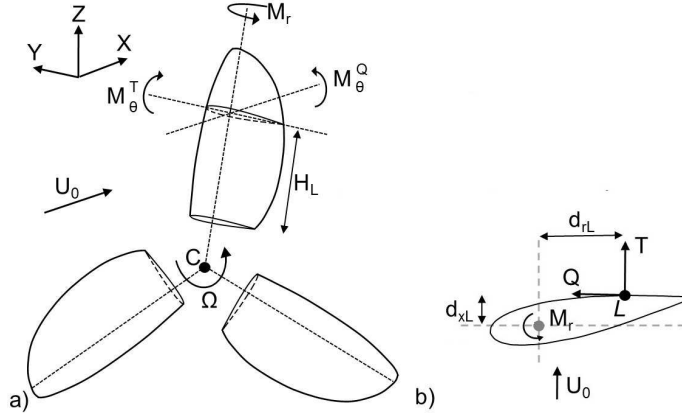

Figure 3: Representation of the bending (M_θ^T and M_θ^Q) and pitching (M_r) moments generated in the HATT. a) Perspective view of the turbine blades. b) Zoom-in of the blade section outlined in a) representing the calculation for the pitching moment.

3.3. Calculation of hydrodynamic loadings on the rotor blades

The blade resolved large-eddy simulations allow the calculation of hydrodynamic loadings on the blade-hub junction, also known as root pitching and bending moments. The latter is considered as a critical turbine design element

10

and probably the most prone to structural failure of the rotor. Here, the hydrodynamic loads are computed directly by integration of the IB nodal forces (Eq. 7). It has to be noted that the blades are considered non-deformable, so the normal forces are not included in the structural analysis.

The total bending moment (M_θ) is calculated from the sum of the bending moments produced by the thrust (T), often named as flapwise moment, and tangential (Q) forces, also called edgewise moment, denoted as M_θ^T and M_θ^Q respectively, as follows,

$$M_\theta = M_\theta^T + M_\theta^Q = \sum_{L=1}^{N_L} T_L \cdot H_L + \sum_{L=1}^{N_L} Q_L \cdot H_L \tag{10}$$

where the lever arm, H_L, is the radial distance between Lagrangian marker L and the blade-hub junction, which is depicted in Fig. 3a).

The torsional or pitching moment, M_r, causes the blades to pitch around the blade-hub junction that induces shear forces, which can lead to structural failure. Analogous calculations are carried out for the contribution of thrust and tangential forces to the total torsional moment using,

$$M_r = M_r^T + M_r^Q = \sum_{L=1}^{N_L} T_L \cdot d_{r_L} + \sum_{L=1}^{N_L} Q_L \cdot d_{x_L} \tag{11}$$

where the lever arms d_{x_L} and d_{r_L} used for thrust and tangential moments respectively, are the distances from the blade cross-section's centre of gravity (C) to the Lagrangian marker position as depicted in Fig. 3b).

The total bending and pitching moments coefficients, denoted as C_{M_θ} and C_{M_r} respectively, are calculated with,

$$C_{M_\theta} = C_{M_\theta^T} + C_{M_\theta^Q} = \frac{M_\theta^T}{1/2\rho U_0^2 AR} + \frac{M_\theta^Q}{1/2\rho U_0^2 AR} \tag{12}$$

$$C_{M_r} = C_{M_r^T} + C_{M_r^Q} = \frac{M_r^T}{1/2\rho U_0^2 AR} + \frac{M_r^Q}{1/2\rho U_0^2 AR} \tag{13}$$

where bending (M_θ^T and M_θ^Q) and pitching moments (M_r^T and M_r^Q) are normalised with fluid density (ρ), free-stream velocity (U_0), swept rotor area (A) and rotor radius (R).

11

3.4. Simulation setup

The computational domain presented in Fig. 4 is $L=8D$ long (x-direction), $B=3D$ wide (y-direction), equaling the width of the laboratory flume. It has a domain height that matches the water depth in the laboratory experiment, i.e. $H=1.6D$. The turbine diameter is $D=0.4$m and is the same as the diameter of the laboratory turbine. The device is centred in the cross-section and is placed $1.5D$ away from the inlet. Considering the channel flow to be fully developed upstream of the turbine, $1/7^{th}$ power law vertical and horizontal velocity profiles with a bulk velocity of $U_0=0.76$m/s are prescribed as inflow condition at the upstream end of the domain. The Reynolds number based on the turbine rotor's diameter ($Re_D = U_0 \cdot D/\nu$) is $3.04 \cdot 10^5$ and the Froude number ($Fr = U_0/\sqrt{g \cdot H}$) is 0.3. No-slip boundary conditions are employed at the side and bottom channel walls while a rigid lid slip condition is used at the water surface. At the downstream end of the domain a convective outflow boundary condition is employed.

The entire domain is decomposed into 720 sub-domains and the division is sketched out via dashed lines in Fig. 4a). Local mesh refinement using three resolution levels (Fig. 4b)) is employed with the goal to achieve an adequate resolution in the proximity of the rotor, while a coarser mesh away from it is needed to make the simulation affordable on the available computational resources. The turbine is rotated for three revolutions as the generated torque converges after approximately one revolution, as demonstrated in Fig. 5a). The simulations are then continued for another two revolutions to obtain average quantities. The simulations are performed on 144 cores on HPC Wales' supercomputer and each simulation consumed approximately 31,000 CPU hours.

3.5. Numerical parameter sensitivity and validation

The method of LES is grid-dependent, i.e. the finer the numerical grid the more length-scales of turbulence are resolved explicitly, and in order to ensure that all relevant turbulent scales are properly resolved it is necessary to carry out at least two LESs on different grids. In addition, and as shown recently [21],
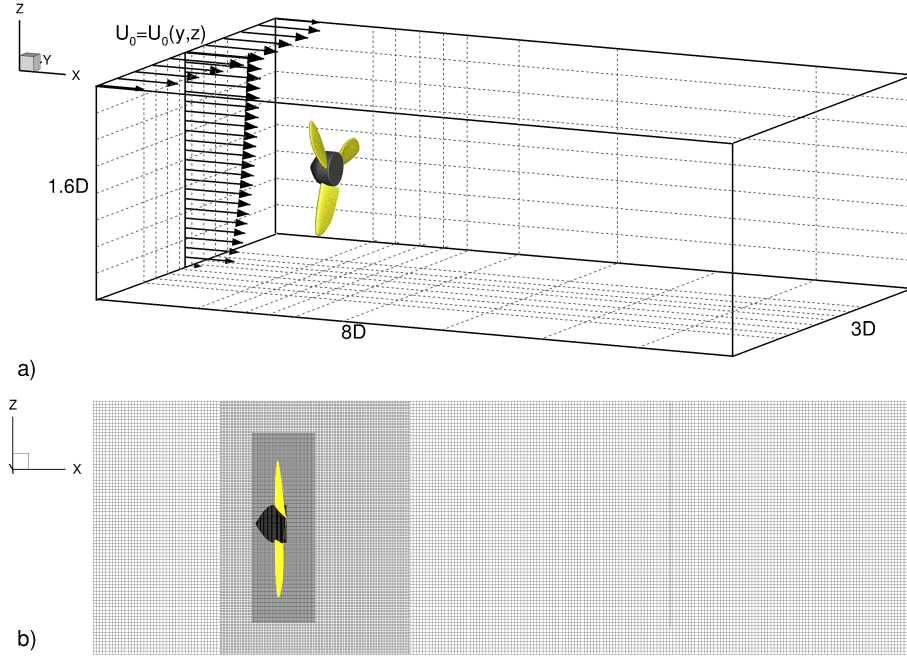
12

Figure 4: a) Numerical domain with the inlet velocity profile sketched; b) Longitudinal plane along y=1.5D (through centre of rotor) showing the mesh distribution with increased resolution around the rotor using local mesh refinement.

the chosen IB method requires a sufficiently fine mesh near the boundaries and small time steps. Here, simulations with two different mesh resolutions and three different time steps are performed. The details of each mesh, which is uniform in the three spatial directions, are provided in Table 1 and refer to the Eulerian mesh resolution at the finest level. The sensitivity of the time step is evaluated on the finest mesh and at rotational speed $\lambda = \lambda_{opt}$ at which the turbine performance is maximum. Fixed time steps of Δt_1=15.0·10^{-5}s, Δt_2=9.0·10^{-5}s, Δt_3=7.5 ·10^{-5}s are tested. The CFL condition based on the rotor's tip-speed ($CFL = U_{tip}\Delta t/\Delta x$, where $U_{tip} = \Omega R$), is CFL=0.036, 0.0216 and 0.018 respectively, small enough to resolve the relevant and most energetic turbulent scales in the flow.

Due to the commercial sensitivity of the experimental data, the computed torque, power coefficient and tip-speed ratio are normalised by the experimental

13

Mesh	$\Delta \mathbf{x}$ (m)	Sections along blade	Blades markers	Hub markers
I	0.0015	100	55110	25642
II	0.0010	150	113775	44006

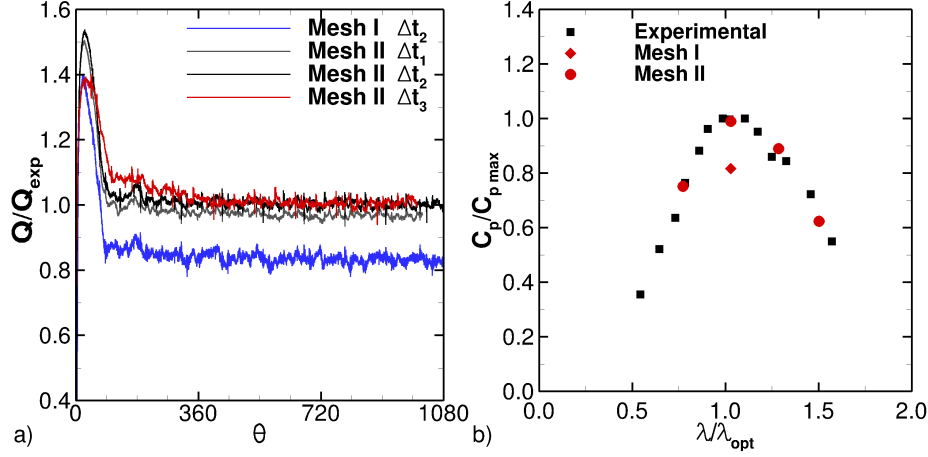Table 1: Details of the meshes used during the spatial resolution sensibility study

Figure 5: a) Instantaneous normalised torque along 3 revolutions with the turbine rotating at $\lambda{=}\lambda_{opt}$ when using different meshes and time steps. b) Normalised computed power coefficient compared to the experimental results for the four different tip-speed ratios analysed.

torque value T_{exp}, the experimental maximum power coefficient $C_{p_{max}}$ and the
tip-speed ratio λ_{opt} at which $C_p{=}C_{p_{max}}$, respectively. The normalised torque
obtained from the simulations on the different meshes and time steps are plotted
as a function of rotated angle in Fig. 5a). The normalised mean power coefficient
is presented in Fig. 5b) as a function of normalised tip-speed ratio for the two
meshes using Δt_2. It is observed that the impact of the mesh resolution is
quite considerable, the simulation on the coarse mesh predicts approximately
20% less torque than the simulation on the fine grid, and this is reflected in
the normalised power coefficient in Fig. 5b). In contrast to this, the effect of
the time step on the fine mesh is relatively small: the simulation using Δt_1
predicts only 3% less torque than the simulations employing Δt_2 or Δt_3. Four
simulations on the finest mesh using Δt_2 are performed covering four different

14

normalised tip-speed ratios, λ/λ_{opt}, so that the turbine characteristic curve can be plotted. As seen from Fig. 5b), the computed normalised power coefficient shows very good agreement with the one obtained from the experiments for all values of λ/λ_{opt}, confirming the accuracy of the method.

4. Results and Discussions

4.1. Hydrodynamics during turbine operation

The complex flow past the tidal turbine rotor is visualised in Fig. 6 depicting instantaneous pressure iso-surfaces (using $p{=}0$), a commonly accepted method to educe coherent flow structures [43]. The helicoidal tip vortices are generated as a result of the shear layer roll-up between the fast flow just above tip of the blade, and the low velocity wake downstream of the rotor. The helicoidal tip vortices are comparable with the ones visualised experimentally by Chamorro et al. [44] and in the LES from Kang et al. [15]. As Fig. 6 suggests, these structures are quite coherent and persist over a considerable period of time: the first vortex generated by blade 1, here denoted as vortex 1b, is still fairly intact while vortex 1a is procreated. The tip vortices are constantly being convected downstream and their spacing, η, is approximately, $\eta = U_b \times 2\pi/\Omega/3$. Between the tip vortices and the hub there is an area of high, quite incoherent turbulence, in the form of small-scale trailing edge turbulence.

The (shortened) hub creates a recirculation zone immediately downstream and a distinct low momentum inner wake, in the form of a spiral vortex, as is depicted in Fig. 6. This inner vortex starts to meander at about two turbine diameters downstream, approximately where the tip vortices lose their coherence and which appears to allow greater entrainment of ambient flow into the wake. Fig. 7a) presents contours of the instantaneous streamwise velocity in a horizontal plane at $z/H = 0.42$ together with streamlines, which indicate that the inner wake rotates clockwise in contrast to the counter-clockwise rotation of the rotor. The inner wake is characterised by low streamwise velocities and pockets of low streamwise velocity are also found inside the tip vortices. In Fig. 7b) flow
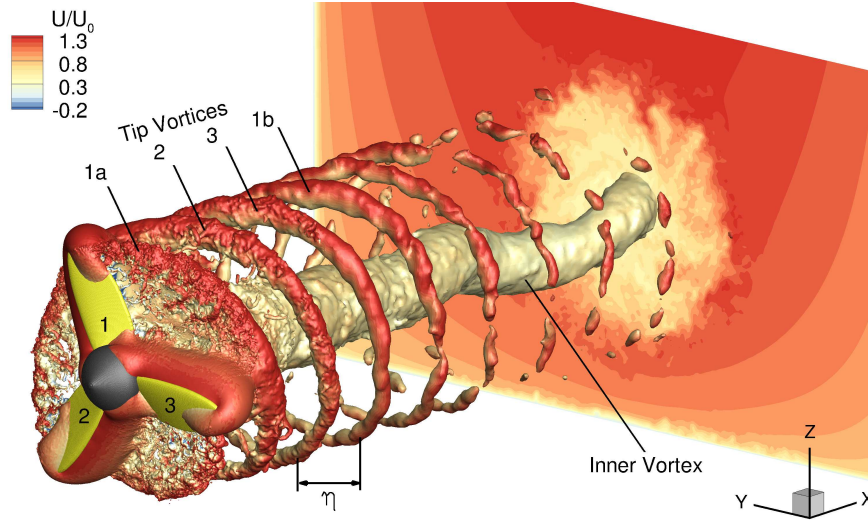
15

Figure 6: Visualisation of the flow structures generated by the turbine rotating at $\lambda=\lambda_{opt}$ represented by $p=0$ iso-surfaces and coloured with the instantaneous non-dimensional streamwise velocity.

structures, visualised using iso-surfaces of λ_2, are plotted together with contours of the instantaneous streamwise velocity in a horizontal plane cutting through the middle of the turbine (at z/H=0.5). The tip vortices are skewed as they are convected downstream by the flow. In addition, smaller, elongated rollers are generated in the shear layer at the edge of the inner wake and are also being convected downstream with the wake.

4.2. Hydrodynamic loadings at the blade-hub juncture

The aim of this section is to quantify bending and torsional moments at the blade root, a critical structural juncture with regards to the survivability of the rotor [45]. The present study analyses the contribution of both thrust and tangential forces to these moments, previously defined in Section 3.3. The former is due to the action of the oncoming fluid onto the turbine's rotor and the latter is mainly caused by the rotational movement of the blades. The value of these moments are obtained for the four simulated tip-speed ratios as they are expected to vary with the rotational speed of the rotor.
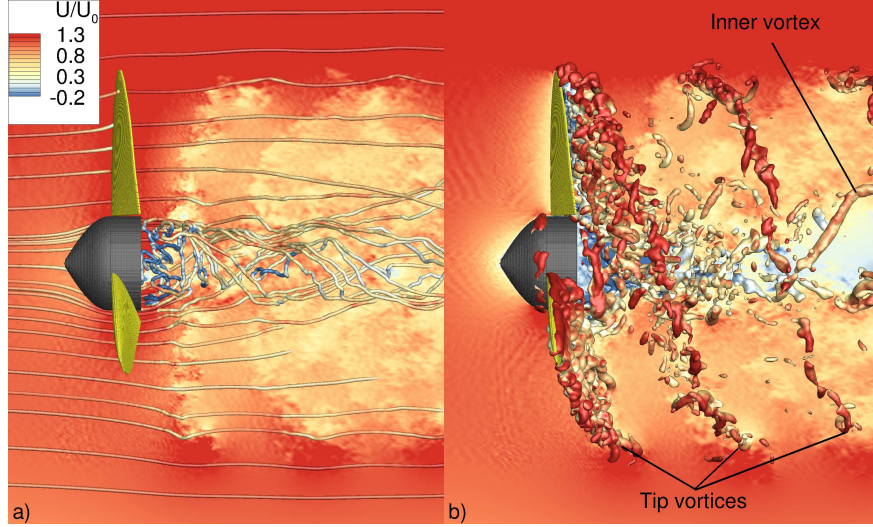
16

Figure 7: Top view of the HATT rotating at $\lambda=\lambda_{opt}$. a) 3D streamlines and vertical contour plane at z/H=0.42 both coloured with the non-dimensional instantaneous streamwise velocity. b) Generated flow structures afterwards the turbine's rotor represented with the λ_2-criterion=800 with a z-plane at z/H=0.50.

²⁷⁵ Fig. 8 shows the instantaneous values of the structural moment coefficients of one blade during the second and third revolutions ($360° < \theta < 1080°$) when the turbine is rotating at λ=0.75, 1.00 and 1.25λ_{opt}. The distribution of the coefficients oscillate sinusoidally and the curve exhibits clear peaks and troughs every 360°. The blade tip is at the top when θ=360°, 720° and 1080° and it ²⁸⁰ is at these angles when the blade experiences the maximum bending moments, as seen in Fig. 8a) and b). At this location the highest velocity occurs in the channel due to the logarithmic/exponential distribution of velocity in open-channel as can be seen from the velocity contours in the cross-section plotted in Fig. 6. Bending moments are smallest when the blade tip is at the lowest point ²⁸⁵ in the water column, which is where the streamwise velocities are lower than near the water surface.

Maximum and minimum moment coefficients vary for different tip speeds. From Fig. 8a), the maximum $C_{M_\theta^T}$ values are found at $\lambda=\lambda_{opt}$ and 1.25λ_{opt} and are similar in magnitude. Minima of $C_{M_\theta^T}$ are found at λ=0.75λ_{opt} and

17

at λ_{opt}. With the turbine rotating at λ=0.75λ_{opt} and 1.00λ_{opt} the $C_{M_\theta^Q}$ curves are very similar over the entire rotation. At tip-speed ratio λ=1.25λ_{opt} the magnitude of $C_{M_\theta^Q}$ drops by approx. 30%, which might be also related with the decrease on the turbine's performance compared to the other tip-speed ratios. This reflects the non-linearity of the flow around tidal turbines and suggests that the structural design of tidal turbines requires the consideration of a range of tip-speed ratios keeping in mind that tidal turbines overspeed/underspeed in tidal environments.
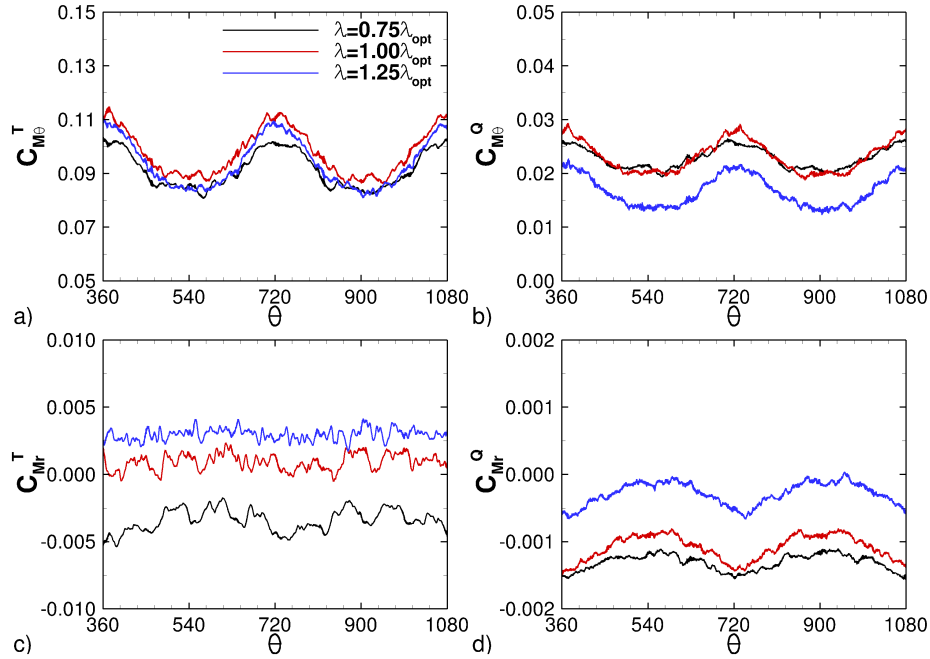

Figure 8: Evolution along the second and third revolutions ($360° < \theta < 1080°$) when the turbine rotates at λ=0.75, 1.00 and 1.25λ_{opt} of: the bending moment coefficients due to a) thrust ($C_{M_\theta^T}$) and b) tangential ($C_{M_\theta^Q}$) forces, and the pitching moments coefficients due to c) thrust ($C_{M_r^T}$) and d) tangential ($C_{M_r^Q}$) forces.

Fig. 8c) and d) demonstrates that the torsional moments are approximately one to two orders of magnitude lower than the bending moments. The pattern of $C_{M_r^T}$ along the two revolutions, plotted in Fig. 8c), does not oscillate sinusoidally and it is quite notably a function of rotational velocity. It is negative and

greatest for $\lambda=0.75\lambda_{opt}$ and nearly zero for $\lambda=\lambda_{opt}$. The distribution of $C_{M_r^T}$, as depicted in Fig. 8d) exhibits a sinusoidal pattern, and is largest (and negative) for $\lambda=0.75\lambda_{opt}$. The tangential forces contributing to the pitching moment coefficient $C_{M_r^Q}$ are smaller than the moments from thrust $C_{M_r^T}$. The difference is mainly due to the length of the lever arm d_{r_L} (see Eq. 11), shown in Fig. 3b), which can be up to 0.75 times the chord length (c) of the blade while d_{x_L} values are based on half the blade thickness and this is much smaller than c.
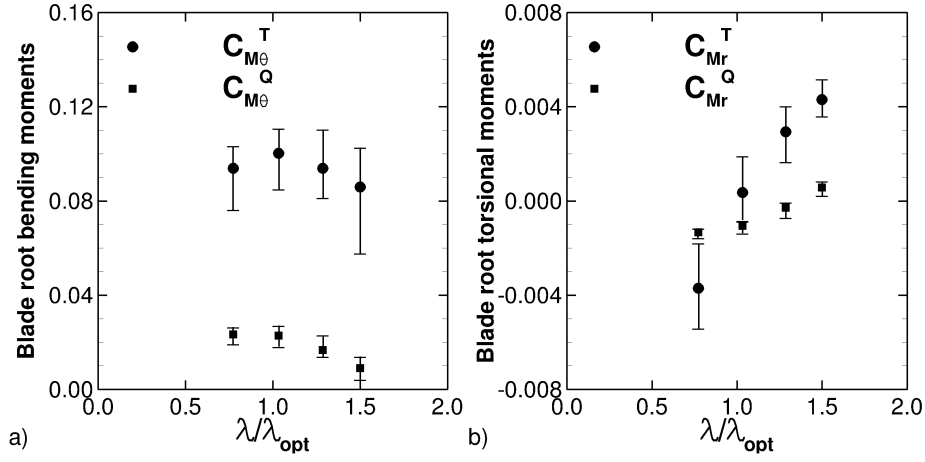

Figure 9: Average value and fluctuation range of the a) blade root bending moment coefficients, $C_{M_\theta^T}$ and $C_{M_\theta^Q}$, and b) the blade root torsional moment coefficients, $C_{M_r^T}$ and $C_{M_r^Q}$.

The averaged values of bending and torsional moment coefficients obtained at various tip-speed ratios are presented in Fig. 9a) and b) and are plotted with their range of fluctuation bounded by the maximum and minimum values. The distribution of bending moments ($C_{M_\theta^T}$ and $C_{M_\theta^Q}$) as a function of tip-speed ratio is similar to the C_P curve and maximum values are found at $\lambda = \lambda_{opt}$. Noteworthy is the fact that the greatest difference between maximum and minimum bending moment is obtained at $\lambda = 1.25\lambda_{opt}$, the highest rotational speed considered herein. This is in line with the experimental results of Blackmore et al. [6]. The thrust component, $C_{M_\theta^T}$, contributes almost 80% to the total bending moment at the root and exhibits greater variation than $C_{M_\theta^Q}$. There are no experimental data to validate the numerically predicted moments, yet

320 Milne et al. [25] and Blackmore et al. [6] reported very similar values from their experimental campaigns for $C_{M_\theta^T} \approx$0.09-0.12 and $C_{M_\theta^Q} \approx$0.01-0.025.

The two averaged torsional moment coefficients, C_{M_r}, increase with an increase in tip-speed ratio as Fig. 9b) shows. At the lowest simulated tip-speed ratio ($\lambda = 0.75\lambda_{opt}$), $C_{M_r^T}$ attains a negative value compared to positive values

325 at higher rotational speeds and the range of fluctuations is fairly inconsistent without a clear sinusoidal pattern. However, the values of $C_{M_r^T}$ are very low. Average values of $C_{M_r^Q}$ are around zero and the curve exhibits a sinusoidal shape as well. However, torsional moments from tangential forces are than the those from thrust forces.

330 *4.3. Effect of free-stream turbulence on rotor hydrodynamics*

The turbine rotor is now subjected to a turbulence intensity (I) of 10%, similar to the one obtained from the experimental velocity signal (see Fig. 2). The turbulence intensity is added to the mean velocity at the inlet via turbulent fluctuations generated using the Synthetic Eddy Method (SEM) from Jarrin et

335 al. [46], considering an eddy length, l_e, value of $0.25H$. The effect of free-stream turbulence on the rotor performance, the wake downstream of the rotor, and the structural bending moments is assessed. In this analysis, only the case with the HATT rotating at $\lambda = \lambda_{opt}$ is simulated using mesh II and Δt_2. The simulation is run for 7 revolutions (θ=2520°). In order to allow comparison of

340 turbulence statistics, the uniform inflow simulation ($I = 0\%$) is run for another 4 revolutions. The flow statistics of the simulations are not fully converged, as they would require running for at least 10 more revolutions, which was deemed too expensive. However, with the chosen period of simulation time differences in the turbine hydrodynamics and structural loadings with and without free-

345 stream turbulence are obvious.

The time-averaged normalised streamwise velocity ($\overline{U}/U_0$) contours in the XY-plane through the middle of the channel depth, i.e. z/H=0.5, are shown in Fig. 10a) and c) for the I=0% and 10% case respectively. These contour plots demonstrate that the wake recovery is shortened due to the presence of free-

20

stream turbulence. The low velocities, represented by the yellow areas, extend
to x/D≈3.5 downstream the turbine for the uniform inlet case, while for the
I=10% case this is reduced to x/D≈1.5. This agrees well with the experimental
findings of Mycek et al. [47], who reported that the velocity deficit recovery in
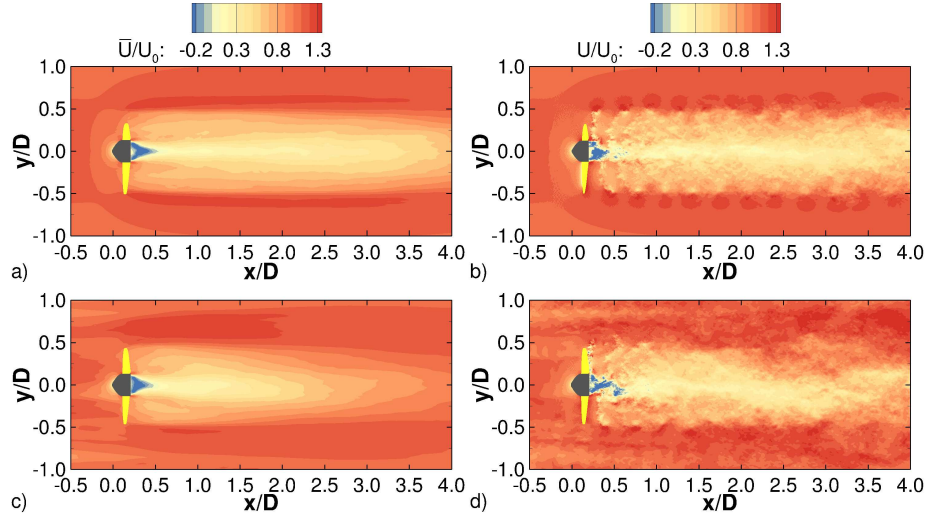the turbine's wake is faster when the turbulence intensity is increased.

Figure 10: XY-planes at the middle of the channel (z/H=0.5) representing the turbine's wake
after rotating 2240°. a) Mean and b) instantaneous non-dimensional streamwise velocity for
the uniform inflow, and c) mean and d) instantaneous non-dimensional streamwise velocity
for the I=10% inflow.

XY-planes of the instantaneous normalised streamwise velocities (U/U_0) are
presented in Fig. 10b) and d) after the turbine rotated 2440°. The tip vortices
are appreciated in the turbine's wake along y/D=-0.5 and 0.5 and high-velocity
pockets above the tip vortices are discerned irrespective of the approach flow
velocity. However, the signatures of the tip vortices are observable until x/D≈3.0
in the uniform inlet case, Fig. 10b), whereas in the presence of free-stream
turbulence the tip vortices are obvious only until x/D≈1.5, see Fig. 10d). The
oncoming turbulence and shear promotes the filling of the low-momentum wake
behind the rotor and results in the shearing and stretching of the tip vortices
and leads to a loss of their coherence. Also, the instantaneous velocity contours

21

of Fig. 10b) and d), suggest that the rotor's wake experiences an earlier onset of meandering in the presence of free-stream turbulence compared to the uniform inlet case. The wake instability is visible already after x/D≈1.5 for the former while the wake becomes unstable at x/D≈3.0 for the latter case. The absence of turbulence in the flow sustains the shear layer between outer flow and rotor wake, and hence promotes a delay of wake meandering. The opposite is found for the I=10% case where after x/D≈1.5 the entrainment of ambient flow into the wake triggers the rotor's wake instability.

The present computational domain, that represents the hydraulic flume, extends vertically 1.6 times the turbine's diameter with a clearance of 0.3D between the blade tips and both the flume's bottom and water surface. This setup results in a notable variation of the hydrodynamics in the vertical direction and this is observable in the normalised streamwise velocity distribution in a longitudinal plane along the channel centre (y/B=0.5) presented in Fig. 11. The normalised time-averaged streamwise velocities contours are presented in Fig. 11a) and c), for the uniform and turbulent inlet velocity conditions respectively, and they show that in both cases the velocity above the turbine (z/D≥0.5) is considerably higher than below it (z/D≤0.5). The difference in wake recovery, already observed in the XY-planes from Fig. 10a) and c), is again appreciated in Fig. 11a) and c). Noteworthy is that the turbine's low momentum wake tends to be filled more noticeably near the bed, in particular for the free-stream turbulence case as seen from Fig. 11c). The channel bed induced turbulence aids in entraining fluid into the wake and this is in line with the findings by Vybulkova et al. [48] who investigated the effects of a parabolic approach flow velocity distribution on the wake of a HATT in comparison with an uniform approach flow.

From the instantaneous normalised streamwise velocity contours of the I=0% case presented in Fig. 11b), the tip vortices are easier to discern than in the I=10% case, plotted in Fig. 11d), and the high velocity pockets are more noticeable near the channel bed, where velocities are generally lower than near the water surface. As described before, the wake of the turbulent inflow case
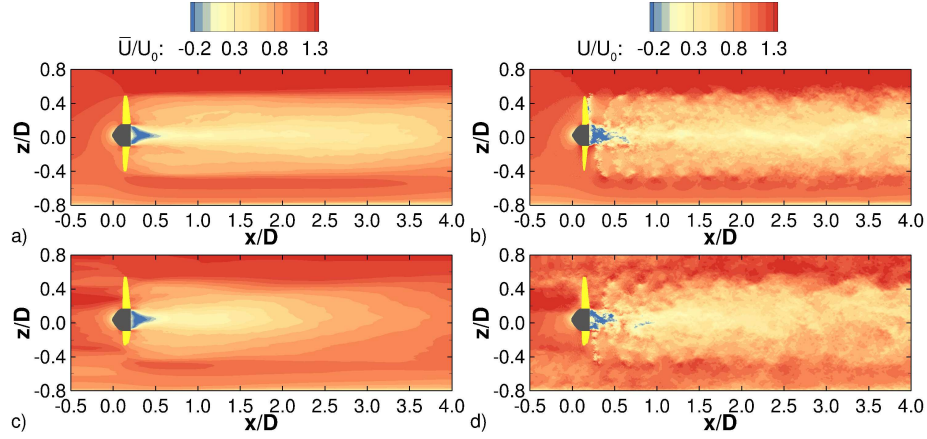
22

Figure 11: XZ-planes at the middle of the channel (y/B=0.5) representing the turbine's wake after rotating 2240°. a) Mean and b) instantaneous normalised streamwise velocity for the uniform inflow (I=0%), and c) mean and d) instantaneous non-dimensionalised streamwise velocity for the turbulent inflow (I=10%).

recovers quicker than the wake for I=0% and it is characterised by a more intense mixing between the free-stream flow and the turbine's wake. The velocity variation over the vertical direction results in an asymmetric filling of the low-momentum turbine which appears to contribute to the meandering of the inner vortex visualised in Fig. 6.

Fig. 12 plots the velocity deficit, U_D, which is defined as $U_D = (U_0 - \overline{U})/U_0$, giving more quantitative evidence of the wake recovery. The U_D profile is steeper for approach flows with greater I, in other words, the flow recovers quicker when the approach flow turbulence intensity is greater. This agrees well with the experimental findings of Mycek et al. [47] and Myers et al. [49], and results from numerical simulations using actuator disk theory from Blackmore et al. [50], who reported that the velocity deficit recovery in the turbines wake is faster when the turbulence intensity is increased. The numerical and experimental data points don't agree perfectly, which is due to the fact that other factors, e.g. flow blockage or incoming flow speed, affect wake recovery as well. However, the figure gives an indication of potential spacing in a turbine farm arrangement and in a highly turbulent environment turbine spacings between 5D and 8D
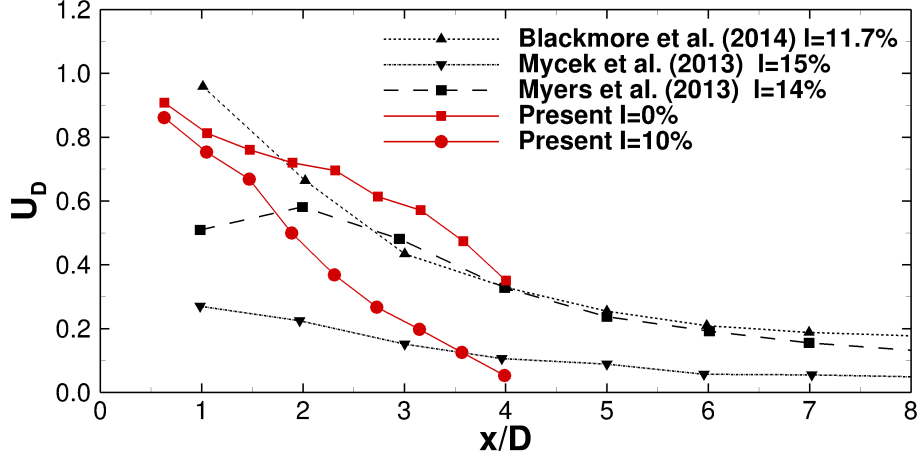
23

Figure 12: Profiles of the velocity deficit in the turbine's wake as simulated by the LES for turbulent and non-turbulent inflow conditions plotted together with data from various other studies.

downstream appear reasonable.

The velocity fluctuations in the turbine's wake are quantified by means of the normalised time-averaged Turbulent Kinetic Energy (TKE), denoted as $\overline{\text{TKE}}=0.5(\overline{u^2}+\overline{v^2}+\overline{w^2})$ where $u=\overline{U}-U$ stands for the velocity fluctuation, and the normalised instantaneous TKE, defined as $\text{TKE}=0.5(u^2+v^2+w^2)$. Both variables are normalised by U_0^2. Contours of $\overline{\text{TKE}}$ and TKE in a longitudinal XZ-plane through the centre of the cross-section are presented in Fig. 13. Contours of normalised $\overline{\text{TKE}}$ for the I=0% and 10% cases are plotted in Fig. 13a) and c) respectively, showing small differences in the $\overline{\text{TKE}}$ distribution until x/D≈1.0. In this near-field area, the signature of the tip vortices is visible with an area of large $\overline{\text{TKE}}$ values (red colour areas) along z/D=-0.5 and z/D=0.5. They are slightly higher for the I=10% case in comparison with the I=0% case due to the ambient turbulence contributing to the velocity fluctuations. Individual tip vortices are easy to discern as pockets of high TKE along z/D=-0.5 and z/D=0.5 in the contours of the instantaneous TKE in the right column of Fig. 13. Downstream of the hub there is an area of elevated TKE until x/D≈0.75 which corresponds to the turbulence in the immediate recirculation zone behind

24

430 the hub's wake.

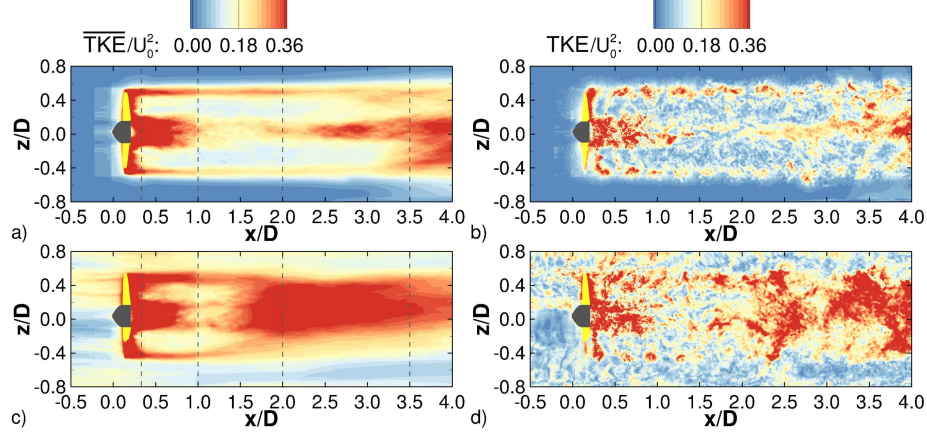

Figure 13: XZ-planes in the centre of the channel (y/B=0.5) of a) Mean and b) instantaneous non-dimensional turbulent kinetic energy for the uniform inflow, and c) mean and d) instantaneous non-dimensional turbulent kinetic energy for the $I{=}10\%$ case.

The most noteworthy difference in the distribution of mean and instantaneous TKE between the turbulent and uniform inflow cases is the far-wake region. An area of high TKE is observed after x/D≈2.5 and x/D≈1.5 for the $I{=}0\%$ and 10% cases respectively. The meandering of the inner vortex, visu-
435 alised in Fig. 6, is responsible for significant velocity fluctuations and hence results in high values of the TKE values. From both, mean and instantaneous TKE plots, it is observed that the wake meandering starts earlier in the $I{=}10\%$ than in the $I{=}0\%$ case and also the magnitude of TKE is greater in the $I{=}10\%$ case. Clearly, the earlier break-down of the tip vortices due to the turbulent am-
440 bient flow leads to an earlier entrainment of fluid into the low-momentum rotor wake and vortex meandering/oscillation appears to be enhanced by the entrainment of turbulent ambient fluid. The turbine's wake analysed and reported herein share several of the characteristics revealed from the LES by Kang et al. [51]. Some of the differences are most likely the result of the higher blockage
445 of the current channel in comparison with their setup.

Fig. 14 presents normalised time-averaged $\overline{\text{TKE}}$ contours in four cross-sections

downstream of the rotor i.e. at x/D=0.33, 1.0, 2.0 and 3.5. These locations are selected to cover the near-wake region (x/D=0.33), the transition between near- and far-wake (x/D=1.0) and the far-wake region for the turbulent inflow case (x/D=2.0) and non-turbulent inflow case (x/D=3.5), respectively. In the near-wake, Fig. 14a) and b), the $\overline{\text{TKE}}$ levels contours are highest in the area of the tip vortices (coinciding with the circumference of the rotor) and in the hub's recirculation zone. There is nearly zero $\overline{\text{TKE}}$ outside of the rotor's swept area in the I=0% case in contrast to the ambient turbulence of the I=10% case. In the intermediate wake region, at x/D=1.0, Fig. 14c) and d), the areas with higher values of $\overline{\text{TKE}}$ look similar among the two cases and the magnitude of $\overline{\text{TKE}}$ is now notably reduced in comparison to x/D=0.33. The decay in velocity fluctuations suggests reduced strength of the tip vortices.
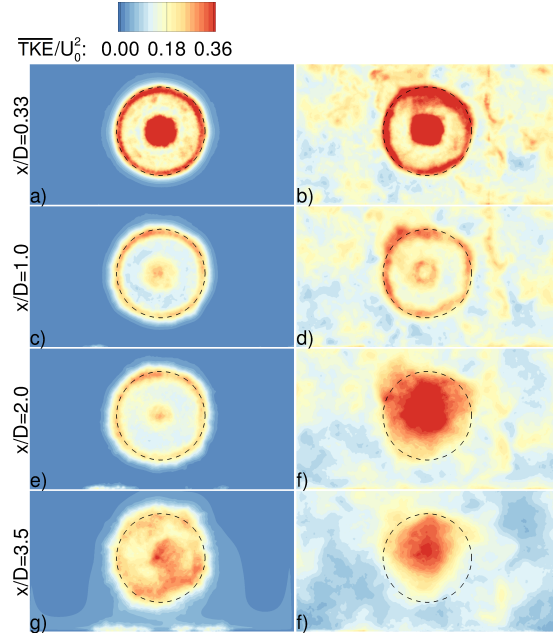

Figure 14: X-planes at 0.33D, 1.0D, 2.0D and 3.5D downstream the turbine representing the normalised mean turbulent kinetic energy contours when an inlet turbulence intensity of I=0% (left column) and I=10% (right column) is used. The dotted circle represents the turbine's swept area.

As seen from Fig. 14e), at x/D=2.0 the $\overline{\text{TKE}}$ distribution and magnitude is very similar than at x/D=2.0, which underlines that the tip vortices remain coherent over a certain period of time in the uniform inflow case. In contrast, the $\overline{\text{TKE}}$ distribution at x/D=2.0 is significantly different from the one at x/D=1.0 for the I=10% case as observed from Fig. 14f). The x/D=2.0 plane can be considered to be already in the far-wake region and therefore high values of $\overline{\text{TKE}}$ are observed in a circular area within the turbine's swept area, as the result of large velocity fluctuations stemming from the meandering of the inner vortex. Noteworthy is the fact that at x/D=2.0 the tip vortices have lost their coherence. In the x/D=3.5 cross-sections, the far-wake developed under turbulent inflow conditions (Fig. 14h)) still exhibits a concentrated region of high $\overline{\text{TKE}}$ albeit the magnitude is reduced compared to x/D=2.0. At this distance downstream of the turbine, the low-momentum zone has been filled with outer fluid and hence the velocity deficit is reduced as also shown in the mean streamwise velocity contours from Fig. 11c). On the contrary, at x/D=3.5 for the uniform inlet case (Fig. 14g)), the unstable far-wake starts to develop with an increase in the $\overline{\text{TKE}}$ levels within the turbine's swept area. At this location the wake does not exhibit the same extent and magnitude of high $\overline{\text{TKE}}$ as in the I=10% case, however the signature of the tip vortices is still visible and this appears to hinder the development of the inner vortex of the I=0% case.

4.4. Effect of free-stream turbulence on hydrodynamic loadings

Fig. 15 presents instantaneous normalised torque as a function of rotation over $180° < \theta < 1260°$ under various inlet turbulence intensities, i.e. I=0%, I=10% and I=20%. The I=20% simulation is added because it represents extreme conditions as observed at the future deployment site of the full-scale tidal turbine. The simulation I=20% is run with exactly the same setup as the I=10% simulation. For the I=0% case, the absence of inflow turbulence results in a smooth almost uniform torque distribution while for the turbulent inflow cases the torque curves describe an oscillating pattern with obvious peaks and troughs. The peaks occur when one blade is at a vertical position with its tip

27

at the uppermost position in the water column. The inflow turbulence affects significantly the instantaneous torque leading to much more variation due to the interaction of the blades with the oncoming turbulent structures, which results in sudden pressure fluctuations on the blades. The higher the inflow turbulence, the stronger the torque fluctuates about the time-averaged value which was also observed by McCann [45]. Despite the obvious difference in the distribution of instantaneous torque, the average power coefficient achieved with $I=10\%$ and $I=20\%$, respectively, is almost identical to the one obtained with a uniform inflow. This is in line with the findings from Mycek et al. [47] who tested experimentally a tidal turbine under two free-stream turbulence intensities of 3% and 15%. They concluded that the turbine experiences only little variation in its performance when the turbulence intensity is increased while large differences were observed in the wake recovery (as shown above).
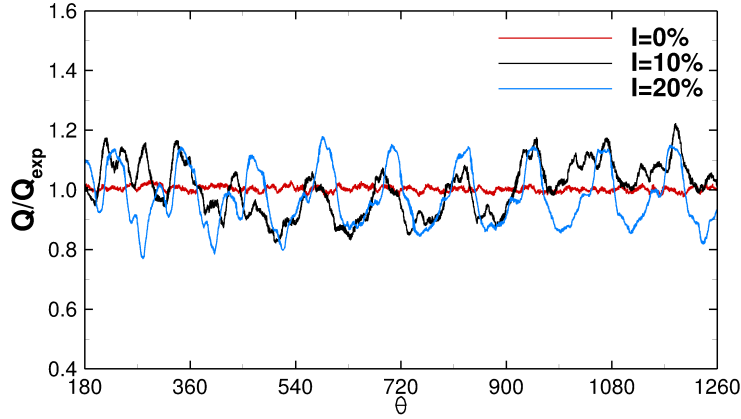

Figure 15: Instantaneous normalised torque value along $180° < \theta < 1260°$ when $I = 0\%$, $I = 10\%$ and $I = 20\%$ are prescribed at the inflow.

The instantaneous bending and torsional coefficients for one blade over $180° < \theta < 1260°$ when using uniform or turbulent inflows is shown in Fig. 16. All structural coefficients obtained from the two turbulent inflow cases follow basically the same patterns as the ones obtained from the zero inlet turbulence case, i.e. a sinusoidal distribution around a mean value. However, the interac-

28

tions of the blade with the oncoming turbulent flow provoke considerable instantaneous variation of the moment coefficients for both turbulent inflow cases. For instance sudden moment fluctuations are appreciated at $\theta \approx 360°$, $\theta \approx 720°$ and $\theta \approx 1080°$ for all four coefficients, and in particular for the $I = 20\%$ exhibiting extreme troughs and peaks. For both $I = 10\%$ and $I = 20\%$ a trough is followed quickly by a peak, a reflection of the vortical motion of the flow. Such sudden variations in hydrodynamic loading due to the oncoming turbulence will result in violent and repeated force accelerations on the blade that could consequently lead to material fatigue and eventually to blade failure.

A quantitative comparison of the peak, average, and the range (defined as range = maximum - minimum) of structural moment coefficients for all cases is possible with the help of Table 2. The magnitudes of the time-averaged moment coefficients are very similar irrespective of the approach flow turbulence intensity. However, the peaks and the ranges, and in particular the bending moment coefficients, are not. Most noteworthy is the significant increase of the peaks of the bending moments of almost 30% for $C_{M_\theta^T}$ and $C_{M_\theta^Q}$ in peak values of the bending moment coefficient with $I{=}10\%$ and almost a 50% increase of the peak value of $C_{M_\theta^T}$ and $C_{M_\theta^Q}$ when $I{=}20\%$. The maximum bending moment coefficient from tangential forces, $C_{M_\theta^Q}$, is considerably smaller than the one from the thrust force, $C_{M_\theta^T}$. The increase in extreme loadings during turbulent approach flows is translated into a wider range of load values as is quantified in Table 2 through the "range" variable. Again higher approach flow turbulence intensity translates into a wider (greater) range, which needs to be sustained by the rotor blades and this has to be taken into consideration during the design process to avoid future failures. The pitching moment coefficients are generally one to two orders of magnitude lower than the bending moments, and the difference in the peaks and ranges between the non-turbulent and the moderately turbulent ($I{=}10\%$) are insignificant. However, a further increase of approach flow turbulence from $I{=}10\%$ to $I{=}20\%$ results in significant increases of the peaks and ranges of pitching moments, i.e. 30% or 50%, respectively.
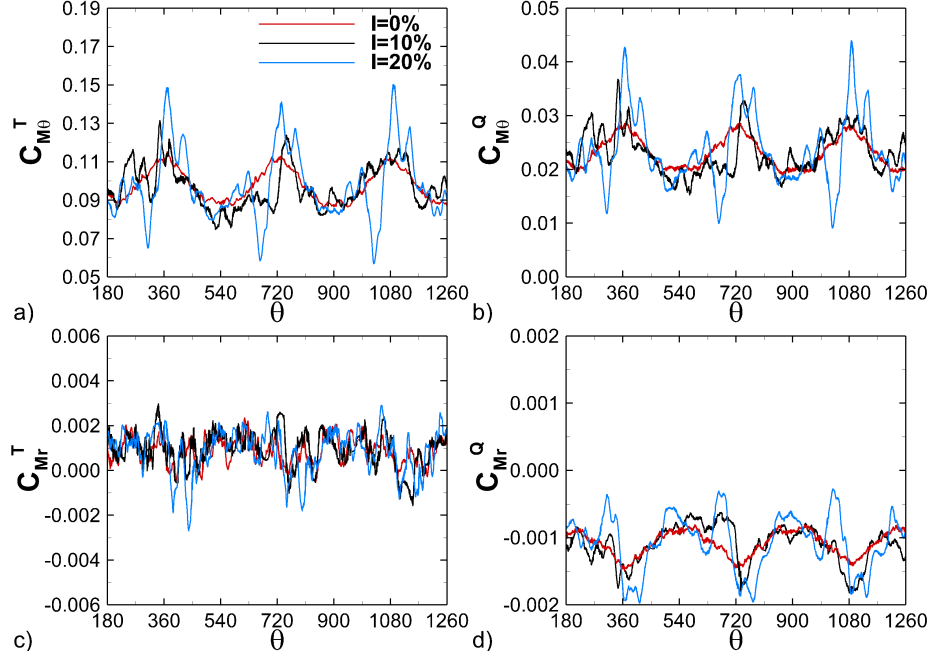
29

Figure 16: Moment coefficients during $180° < \theta < 1260°$ of rotation under different free-stream turbulence intensities and when the turbine rotates at $\lambda = \lambda_{opt}$. Bending moment coefficients due to thrust (a) and tangential forces (b), and pitching moment coefficients due to axial forces (c) and tangential forces (d)

5. Conclusions

The method of large eddy simulation together with the immersed boundary method has been employed to study the hydrodynamics and resulting loads of a horizontal axis tidal turbine prototype. The numerical method was validated first and the sensitivity of the spatial and temporal resolution was assessed first with the goal of determining the optimum numerical setup in terms of time step and mesh size. It has been shown that the simulation in terms of the resulting torque is less sensitive to the time step than the mesh size. Numerically predicted power coefficients at various tip-speed ratios agreed well with experimental data provided an adequately fine numerical mesh is employed. After successful validation of the method, further simulations were run with the goal to investigate the turbine's hydrodynamics and the resulting loadings on its

30

Moment Coefficient	Value	I=0%	I=10%	I=20%
$C_{M_\theta^T}$	peak	0.111	0.131	0.150
	mean	0.100	0.096	0.098
	range	0.026	0.055	0.093
$C_{M_\theta^Q}$	peak	0.0276	0.0365	0.0437
	mean	0.0228	0.0230	0.0235
	range	0.0090	0.0206	0.0346
$C_{M_r^T}$	peak	0.0020	0.0021	0.0029
	mean	0.0004	0.0010	0.0010
	range	0.0012	0.0013	0.0026
$C_{M_r^Q}$	peak	-0.00146	-0.00179	-0.00199
	mean	-0.00106	-0.00146	-0.00108
	range	0.00067	0.00065	0.00172

Table 2: Peak, mean, and range of bending and pitching moment coefficients under flows of different turbulence intensity.

blades. The analysis of the simulation data in terms of hydrodynamics revealed the typical flow structures of horizontal axis turbines, including tip vortices and an inner, counter-rotating vortex, which were visualised using common turbulence structure eduction methods. In terms of hydrodynamic loads, bending and torsional moment coefficients at the blade-hub junction were computed for different tip-speed ratios. The results show that there is a considerable fluctuation of the structural moments over one revolution, mainly due to the turbine's operation in a boundary layer flow. It has also been demonstrated that the tip-speed ratio at which the turbine operates has an effect on the magnitude of the coefficients, most noteworthy that the largest bending moments occur when the turbine operates at the peak of the power curve.

With the goal of reproducing more realistic environmental conditions, the turbine rotor was then subjected to the same flow plus additional free-stream turbulence with an intensity of I=10%, which was prescribed at the inlet us-

ing the Synthetic Eddy Method. The results show a notable change of the hydrodynamics of the turbine's wake. Under free-stream turbulent conditions, the velocity deficit reduces quicker than under uniform inflow conditions. It is shown that an increase in ambient turbulence reduces the longevity of the tip-speed vortices but also that the onset of inner vortex meandering starts closer to the rotor. The turbine wake is filled quicker at greater turbulence intensity, a result of the additional shear in the flow. From contours of the time-averaged and instantaneous turbulent kinetic energy distribution three wake regions have been distinguished: a near-field wake with distinct signatures of the tip vortices and the recirculation zone behind the hub, an intermediate wake with fairly low turbulence and a far-field wake an area of high TKE as a result of the meandering of the wake. Ambient turbulence affects the TKE levels and the extent of the three regions: at high levels of ambient turbulence significantly elevated turbulence in the far-field wake and earlier onset of wake meandering were found.

Analysis of the effects of ambient turbulence on hydrodynamic loadings has revealed that the mean structural coefficients are fairly similar irrespective of the level of ambient turbulence. However, the peak values and the range (i.e. the difference between maximum and minimum value) of the structural coefficients are increased due to turbulence. It has been shown that in the presence of turbulent flow structures can lead to sudden changes in the hydrodynamic loadings, and in particular for high ambient turbulence, minima are followed directly by maxima of the moment coefficients. High levels of ambient turbulence, such as found at a future turbine deployment site can result in a 50% increase of instantaneous bending and pitching moments. The pitching moments have been found to be one to two orders of magnitude lower than the bending moments.

Acknowledgements

[1] M. Khan, G. Bhuyan, M. Iqbal, J. Quaicoe, Hydrokinetic energy conversion systems and assessment of horizontal and vertical axis turbines for river and tidal applications: A technology status review, Appl. Energy 86 (10) (2009) 1823–1835. `doi:10.1016/j.apenergy.2009.02.017`.

[2] A. Bahaj, A. Molland, J. Chaplin, W. Batten, Power and thrust measurements of marine current turbines under various hydrodynamic flow conditions in a cavitation tunnel and a towing tank, Renew. Energy 32 (3) (2007) 407–426. `doi:10.1016/j.renene.2006.01.012`.

[3] P. Mycek, B. Gaurier, G. Germain, G. Pinon, E. Rivoalen, Experimental study of the turbulence intensity effects on marine current turbines behaviour. Part II: Two interacting turbines, Renew. Energy 68 (2014) 876–892. `doi:10.1016/j.renene.2013.12.048`.

[4] R. Vennell, S. W. Funke, S. Draper, C. Stevens, T. Divett, Designing large arrays of tidal turbines: A synthesis and review, Renew. Sustain. Energy Rev. 41 (2015) 454–472. `doi:10.1016/j.rser.2014.08.022`.

[5] I. Milne, A. Day, R. Sharma, R. Flay, Blade loading on tidal turbines for uniform unsteady flow, Renew. Energy 77 (2015) 338–350. `doi:10.1016/j.renene.2014.12.028`.

[6] T. Blackmore, L. E. Myers, A. S. Bahaj, Effects of turbulence on tidal turbines: Implications to performance, blade loads, and condition monitoring, Int. J. Mar. Energy 14 (2016) 1–26. `doi:10.1016/j.ijome.2016.04.017`.

[7] J. N. Sorensen, W. Z. Shen, Numerical Modeling of Wind Turbine Wakes, J. Fluids Eng. 124 (2002) 393–399. `doi:10.1115/1.1471361`.

[8] H. Sarlak, C. Meneveau, J. Sørensen, Role of subgrid-scale modeling in large eddy simulation of wind turbine wake interactions, Renew. Energy 77 (2015) 386–399. `doi:10.1016/j.renene.2014.12.036`.

33

[9] J. G. Leishman, Challenges in Modeling the Unsteady Aerodynamics of Wind Turbines, Wind Energy 5 (2002) 85–132. `doi:10.1115/we.62`.

[10] C. Frost, C. Morris, A. Mason-Jones, D. O'Doherty, T. O'Doherty, The effect of tidal flow directionality on tidal turbine performance characteristics, Renew. Energy 78 (2015) 609–620. `doi:10.1016/j.renene.2015.01.053`.

[11] A. Mason-Jones, D. O'Doherty, C. Morris, T. O'Doherty, Influence of a velocity profile & support structure on tidal stream turbine performance, Renew. Energy 52 (2013) 23–30. `doi:10.1016/j.renene.2012.10.022`.

[12] T. Stoesser, Large-eddy simulation in hydraulics: Quo Vadis?, J. Hydraul. Res. 52 (4) (2014) 441–452. `doi:10.1080/00221686.2014.944227`.

[13] M. Visbal, T. O. Yilmaz, D. Rockwell, Three-dimensional vortex formation on a heaving low-aspect-ratio wing: Computations and experiments, J. Fluids Struct. 38 (2013) 58–76. `doi:10.1016/j.jfluidstructs.2012. 12.005`.

[14] F. Sotiropoulos, Hydraulics in the era of exponentially growing computing power, J. Hydraul. Res. 53 (5) (2015) 547–560. `doi:10.1080/00221686. 2015.1119210`.

[15] S. Kang, I. Borazjani, J. A. Colby, F. Sotiropoulos, Numerical simulation of 3D flow past a real-life marine hydrokinetic turbine, Adv. Water Resour. 39 (2012) 33–43. `doi:10.1016/j.advwatres.2011.12.012`.

[16] J. McNaughton, I. Afgan, D. D. Apsley, S. Rolfo, T. Stallard, P. K. Stansby, A simple sliding-mesh interface procedure and its application to the CFD simulation of a tidal-stream turbine, Int. J. Numer. Methods Fluids 74 (4) (2014) 250–269. `doi:10.1002/fld.3849`.

[17] X. Bai, E. Avital, A. Munjiza, J. Williams, Numerical simulation of a marine current turbine in free surface flow, Renew. Energy 63 (2014) 715–723. `doi:10.1016/j.renene.2013.09.042`.

[18] C. Peskin, Flow patterns around heart valves: A numerical method, J. Comput. Phys. 10 (2) (1972) 252–271. `doi:10.1016/0021-9991(72)90065-4`.

[19] E. Fadlun, R. Verzicco, P. Orlandi, J. Mohd-Yusof, Combined Immersed-Boundary Finite-Difference Methods for Three-Dimensional Complex Flow Simulations, J. Comput. Phys. 161 (1) (2000) 35–60. `doi:10.1006/jcph.2000.6484`.

[20] M. Uhlmann, An immersed boundary method with direct forcing for the simulation of particulate flows, J. Comput. Phys. 209 (2) (2005) 448–476. `doi:10.1016/j.jcp.2005.03.017`.

[21] P. Ouro, T. Stoesser, An immersed boundary-based large-eddy simulation approach to predict the performance of vertical axis tidal turbines, Submitt. to Comput. Fluids.

[22] P. Ouro, T. Stoesser, R. McSherry, Large-Eddy Simulation of a Vertical Axis Tidal Turbine using an Immersed Boundary Method, in: CFD Wind Tidal Offshore turbines, Springer International Publishing, 2015, Ch. 5, pp. 49–58. `doi:10.1007/978-3-319-16202-7_5`.

[23] P. Ouro, L. Cea, L. Ramírez, X. Nogueira, An immersed boundary method for unstructured meshes in depth averaged shallow water models, Int. J. Numer. Methods Fluids 81 (11) (2016) 672–688. `doi:10.1002/fld.4201`.

[24] F. Sotiropoulos, X. Yang, Immersed boundary methods for simulating fluidstructure interaction, Prog. Aerosp. Sci. 65 (2014) 1–21. `doi:10.1016/j.paerosci.2013.09.003`.

[25] I. A. Milne, A. H. Day, R. N. Sharma, R. G. J. Flay, Blade loads on tidal turbines in planar oscillatory flow, Ocean Eng. 60 (2013) 163–174. `doi:10.1016/j.oceaneng.2012.12.027`.

[26] R. F. Nicholls-Lee, S. R. Turnock, S. W. Boyd, Application of bend-twist coupled blades for horizontal axis tidal turbines, Renew. Energy 50 (2013) 541–550. `doi:10.1016/j.renene.2012.06.043`.

[27] S. C. Tatum, C. H. Frost, M. Allmark, D. M. O'Doherty, A. Mason-Jones, P. W. Prickett, R. I. Grosvenor, C. B. Byrne, T. O'Doherty, Wave-current interaction effects on tidal stream turbine performance and loading characteristics, Int. J. Mar. Energy 14 (2016) 161–179. `doi:10.1016/j.ijome.2015.09.002`.

[28] M. Harrold, P. Bromley, P. Clelland, D. Broudic, Demonstrating a tidal turbine control strategy at laboratory scale, in: ASME 2016 35th Int. Conf. Ocean. Offshore Arct. Eng., Busan, South Korea, 2016.

[29] S. Tedds, I. Owen, R. Poole, Near-wake characteristics of a model horizontal axis tidal stream turbine, Renew. Energy 63 (2014) 222–235. `doi:10.1016/j.renene.2013.09.011`.

[30] A. Mason-Jones, D. M. O'Doherty, C. E. Morris, T. O'Doherty, C. B. Byrne, P. W. Prickett, R. I. Grosvenor, I. Owen, S. Tedds, R. J. Poole, Non-dimensional scaling of tidal stream turbines, Energy 44 (2012) 820–829. `doi:10.1016/j.energy.2012.05.010`.

[31] A. Mason-Jones, Performance assessment of a horizontal axis tidal turbine in a high velocity shear environment, Phd thesis, Cardiff University (2010).

[32] B. Fraga, T. Stoesser, C. C. Lai, S. A. Socolofsky, A LES-based EulerianLagrangian approach to predict the dynamics of bubble plumes, Ocean Model. 97 (2016) 27–36. `doi:10.1016/j.ocemod.2015.11.005`.

[33] B. Fraga, T. Stoesser, Influence of bubble size, diffuser width and flow rate on the integral behaviour of bubble plumes, J. Geophys. Res. Ocean.`doi:10.1002/2015JC011381`.

[34] S. Kara, T. Stoesser, T. W. Sturm, Turbulence statistics in compound channels with deep and shallow overbank flows, J. Hydraul. Res. 50 (5) (2012) 482–493. `doi:10.1080/00221686.2012.724194`.

[35] M. C. Kara, T. Stoesser, R. McSherry, Calculation of fluidstructure interaction: methods, refinements, applications, Proc. ICE - Eng. Comput. Mech. 168 (2) (2015) 59–78. `doi:10.1680/eacm.15.00010`.

[36] S. Kara, M. C. Kara, T. Stoesser, T. W. Sturm, Free-Surface versus Rigid-Lid LES Computations for Bridge-Abutment Flow, J. Hydraul. Eng. 141 (9) (2015) 04015019. `doi:10.1061/(ASCE)HY.1943-7900.0001028`.

[37] S. Kara, T. Stoesser, T. W. Sturm, S. Mulahasan, Flow dynamics through a submerged bridge opening with overtopping, J. Hydraul. Res. 53 (2) (2015) 186–195. `doi:10.1080/00221686.2014.967821`.

[38] F. Nicoud, F. Ducros, Subgrid-scale stress modelling based on the square of the velocity gradient tensor, Flow, Turbul. Combust. 62 (3) (1999) 183–200. `doi:10.1023/A:1009995426001`.

[39] R. Verzicco, P. Orlandi, A Finite-Difference Scheme for Three-Dimensional Incompressible Flows in Cylindrical Coordinates, J. Comput. Phys. 123 (2) (1996) 402–414. `doi:10.1006/jcph.1996.0033`.

[40] A. Cristallo, R. Verzicco, Combined Immersed Boundary/Large-Eddy-Simulations of Incompressible Three Dimensional Complex Flows, Flow, Turbul. Combust. 77 (2006) 3–26. `doi:10.1007/s10494-006-9034-6`.

[41] M. Cevheri, R. McSherry, T. Stoesser, A local mesh refinement approach for large-eddy simulations of turbulent flows, Int. J. Numer. Methods Fluids 82 (2016) 261–285. `doi:10.1002/fld.421`.

[42] X. Yang, X. Zhang, Z. Li, G. W. He, A smoothing technique for discrete delta functions with application to immersed boundary method in moving boundary simulations, J. Comput. Phys. 228 (20) (2009) 7821–7836. `doi:10.1016/j.jcp.2009.07.023`.

37

[43] W. Rodi, G. Constantinescu, T. Stoesser, Large-Eddy Simulation in Hydraulics, IAHR Monographs, CRC Press, Leiden, The Netherlands, 2013.

[44] L. P. Chamorro, D. R. Troolin, S. J. Lee, R. E. A. Arndt, F. Sotiropoulos, Three-dimensional flow visualization in the wake of a miniature axial-flow hydrokinetic turbine, Exp. Fluids 54 (2). `doi:10.1007/s00348-013-1459-9`.

[45] G. McCann, Tidal current turbine fatigue loading sensitivity to waves and turbulence a parametric study, in: Proc. 7th Eur. Wave Tidal Energy, Porto, Portugal, 2007.

[46] N. Jarrin, S. Benhamadouche, D. Laurence, R. Prosser, A synthetic-eddy-method for generating inflow conditions for large-eddy simulations, Int. J. Heat Fluid Flow 27 (4) (2006) 585–593. `doi:10.1016/j.ijheatfluidflow.2006.02.006`.

[47] P. Mycek, B. Gaurier, G. Germain, G. Pinon, E. Rivoalen, Experimental study of the turbulence intensity effects on marine current turbines behaviour. Part I: One single turbine, Renew. Energy 66 (2014) 729–746. `doi:10.1016/j.renene.2013.12.036`.

[48] L. Vybulkova, M. Vezza, R. Brown, Simulating the wake downstream of a horizontal axis tidal turbine using a modified vorticity transport model, IEEE J. Ocean. Eng. 41 (2) (2016) 296–301. `doi:10.1109/JOE.2015.2429231`.

[49] L. E. Myers, K. Shah, P. W. Galloway, Design, commissioning and performance of a device to vary the turbulence in a recirculating flume, in: 10th Eur. Wave Tidal Energy Conf., Aalborg, Denmark, 2013.

[50] T. Blackmore, W. Batten, A. S. Bahaj, Influence of turbulence on the wake of a marine current turbine simulator, Proc. R. Soc. A 470 (2014) 20140331. `doi:10.1098/rspa.2014.0331`.

[51] S. Kang, X. L. Yang, F. Sotiropoulos, On the onset of wake meandering for
an axial flow turbine in a turbulent open channel flow, J. Fluid Mech. 744
(2014) 376–403. doi:10.1017/jfm.2014.82.